Research Square

Preprints are preliminary reports that have not undergone peer review.
They should not be considered conclusive, used to inform clinical practice,
or referenced by the media as validated information.

Spatial Support and Operator Structure in GSTAR Models: Administrative Regions versus Regular Grids for Wildfire Hotspot Data

Nur'ainul Miftahul Huda
nurainul@fmipa.untan.ac.id
Tanjungpura University
Yundari yundari
Tanjungpura University
Nurfitri Imro'ah
Tanjungpura University
Rahmi Hidayati
Tanjungpura University
Kartika Sari
Tanjungpura University
Muhammad Yahya Ayyash
Tanjungpura University

Research Article

Keywords: Spatial support, weight matrix structure, grid discretization, administrative aggregation

Posted Date: November 13th, 2026

DOI: https://doi.org/10.21203/rs.3.rs-11459649/v1

License: This work is licensed under a Creative Commons Attribution 4.0 International License.
Read Full License

Additional Declarations: No competing interests reported.

Spatial Support and Operator Structure in GSTAR Models: Administrative Regions versus Regular Grids for Wildfire Hotspot Data

Nur'ainul Miftahul Huda[1*], Yundari[1], Nurfitri Imro'ah[2], Rahmi Hidayati[3], Kartika Sari[3], Muhammad Yahya Ayyash[2]

[1*]Department of Mathematics, Faculty of Mathematics and Natural Sciences, Universitas Tanjungpura, Prof. H. Hadari Nawawi St., Pontianak, 78124, West Kalimantan, Indonesia.
[2]Department of Statistics, Faculty of Mathematics and Natural Sciences, Universitas Tanjungpura, Prof. H. Hadari Nawawi St., Pontianak, 78124, West Kalimantan, Indonesia.
[3]Department of Computer System Engineering, Faculty of Mathematics and Natural Sciences, Universitas Tanjungpura, Prof. H. Hadari Nawawi St., Pontianak, 78124, West Kalimantan, Indonesia.

*Corresponding author(s). E-mail(s): nurainul@fmipa.untan.ac.id;
Contributing authors: yundari@math.untan.ac.id;
nurfitriimroah@math.untan.ac.id; rahmihidayati@siskom.untan.ac.id;
kartikasari@siskom.untan.ac.id; H1091211042@student.untan.ac.id;

Abstract

This study examines the impact of spatial support transformation on the structure and stability of the Generalized Space-Time Autoregressive (GSTAR) framework. We explore two types of spatial representation: irregular administrative regions and regular, high-density grid discretization. Administrative regions are typically defined by polygonal boundaries, and the heterogeneity of these polygons often leads to inconsistent neighborhood configurations and non-uniform spatial interactions. In contrast, regular grid discretization yields more structured, sparse spatial operators. Using spatio-temporal environmental data obtained from NASA FIRMS observations, GSTAR models were constructed using different spatial supports and evaluated based on spatial interaction structure, parameter stability, and forecasting characteristics. Beyond empirical comparison, this study investigates the structural properties of the resulting GSTAR operators, such as sparsity

preservation, block-banded structure, and spectral properties within the regular grid topology. The results indicate that regular grid discretization is more efficient than irregular administrative aggregation at preserving local neighborhood interactions; this method produces spatial operators that are sparser, more localized, and spectrally controlled, which in turn leads to more stable and accurate spatio-temporal parameter estimation. On the other hand, forecasting accuracy proves to be highly dependent on the error measurement method: when compared at the original scale (without standardization), grid-based models yield lower absolute forecasting errors; However, once errors are standardized based on the variability of each spatial unit—an adjustment necessary given that spatially aggregated administrative data series tend to be structurally smoother—administrative support actually yields normalized errors that are comparable or even lower. We present both perspectives and argue that the primary structural advantage of grid support lies in operator sparsity and parameter stability, rather than in an absolute superiority in forecasting accuracy. These results demonstrate that spatial support is not merely a pre-processing step, but a structural element that fundamentally impacts the behavior of spatio-temporal operators.

Keywords: Spatial support, weight matrix structure, grid discretization, administrative aggregation

1 Introduction

Many environmental processes evolve simultaneously in both space and time, and observations at a given location depend on both their own past and the conditions at surrounding locations ([1, 2]). Forest fires are a clear example; they are triggered by various factors, including weather, human activity, and the spread of fire between adjacent areas ([3, 4]). In Indonesia, peatland fires also have serious consequences for the environment and public health ([5, 6]); therefore, models capable of capturing the spatio-temporal dynamics of such phenomena are essential for early warning and mitigation efforts (e.g., [7–9]).

To address this, a model must first define its "spatial support"—that is, how continuous space is partitioned into units within which data are recorded and analyzed ([10]). Most empirical studies use administrative boundaries, which are considered practical and well aligned with existing policy frameworks. However, administrative units vary significantly in size and shape, resulting in an irregular neighborhood structure. This is closely linked to the "Modifiable Areal Unit Problem" (MAUP): different ways of aggregating data—even when using the same underlying dataset—can alter estimates of dependency and the resulting inferences ([11]), and may also affect predictive performance ([12]).

The Generalized Space-Time Autoregressive (GSTAR) model is widely used for spatio-temporal data ([13]). This model is an extension of the Vector Autoregressive (VAR) model, incorporating spatial lags defined via a weight matrix ([14]); consequently, the weight matrix determines how spatial dependence is represented ([15]). Previous research has explored adaptive weights, estimation methods, intervention and

outlier modeling, and various structured weighting schemes ([16]). Furthermore, developments have been made regarding clustering and block-structured representations for heterogeneous environmental data ([14–21]). However, most of these applications involve a small number of locations within a limited geographic area.

As the number of locations increases, the structure of the spatial operator becomes increasingly significant. Administrative regions often yield denser, less regular weight matrices, which can lead to less stable estimates and higher computational costs. In contrast, a regular grid provides a relatively constant number of neighbors for each cell, resulting in a sparse operator that approximates a banded matrix structure ([22, 23]). How the sparsity pattern, block organization, and spectral behavior of the GSTAR operator evolve with changes in spatial support—and the subsequent implications for parameter stability—have received insufficient attention ([24, 25]). While a finer spatial support can preserve local interactions and reduce aggregation bias, it simultaneously increases the dimensionality of the operator.

This paper examines this issue by comparing two types of spatial support for the same dataset: irregular administrative regions and a regular grid. We utilize weekly hotspot count data from NASA FIRMS for the West Kalimantan region, Indonesia, represented either as $N_{\mathcal{A}} = 14$ regencies and cities or as $N_{\mathcal{G}} = 51$ terrestrial cells, each measuring $0.5^\circ \times 0.5^\circ$ (Section 6.1). The contributions of this research are threefold. First, we formalize the "Change of Support Problem" within the GSTAR framework (Section 3.1). Second, we characterize the growth of sparsity, the quasi-banded organization, and the spectral constraints of the GSTAR operator within the context of a grid-based support (Section 4). These properties are derived from established results on row-normalized weight matrices on bounded-degree graphs; however, to the best of our knowledge, they have not been articulated previously for high-dimensional GSTAR models. Third, through simulations and empirical applications, we demonstrate that the choice of spatial support is not a neutral preprocessing step, as it alters the operator's structure and the stability of the estimated parameters (Sections 5–6).

Forecast accuracy is treated as a secondary outcome, and existing evidence is mixed. Raw forecast errors appear to favor grid-based approaches; however, such comparisons are inherently biased because aggregated administrative data series tend to be smoother than grid-level data series. Once these errors are standardized for each unit's variability, the apparent advantage of grid-based approaches diminishes or even reverses. Consequently, the primary contribution of this paper lies in its operator structure and parameter stability, rather than in forecast accuracy.

The remainder of this paper is organized as follows. Section 2 introduces the GSTAR model, the weight matrix, two types of supports, and their theoretical properties. Section 5 presents a simulation study, supplemented by five robustness checks. Section 6 applies the framework to hotspot data, while Section 7 examines the findings. Finally, Section 8 provides the conclusion.

2 Spatio-Temporal Modeling Framework

Terminology.

We call the two spatial representations compared in this study the *administrative support* $\mathcal{A}$ and the *grid support* $\mathcal{G}$, and refer to their individual units as *administrative regions* and *grid cells*. *Administrative aggregation* and *grid discretization* denote only the procedures that construct these supports from finer data. The matrices $\mathbf{W}^{(\ell)}$ are called *spatial operators*, and the composite $\sum_{k,\ell} \mathbf{\Phi}_{k,\ell}\mathbf{W}^{(\ell)}$ is called the *GSTAR operator*.

2.1 General Model Specification

We study how the spatial support changes the propagation of spatio-temporal dependence within the GSTAR framework, which captures temporal persistence and spatial spillover through spatial lag operators built from the neighborhood structure. Let $\mathbf{Z}_t = (Z_{1,t}, Z_{2,t}, \ldots, Z_{N,t})^\top$ be the $N \times 1$ observation vector at time t. The GSTAR model is ([17, 19])

$$\mathbf{Z}_t = \sum_{k=1}^{p} \sum_{\ell=0}^{\lambda_k} \mathbf{\Phi}_{k,\ell}\mathbf{W}^{(\ell)}\mathbf{Z}_{t-k} + \boldsymbol{\varepsilon}_t, \tag{1}$$

where p is the temporal lag order and λ_k is the maximum spatial lag at temporal lag k. The matrices $\mathbf{\Phi}_{k,\ell}$ hold the autoregressive coefficients, $\mathbf{W}^{(\ell)}$ is the spatial operator of order ℓ with $\mathbf{W}^{(0)} = \mathbf{I}$, and $\boldsymbol{\varepsilon}_t$ is a zero-mean innovation with finite covariance. The model extends the Vector Autoregressive (VAR) model with spatially lagged terms. Higher spatial orders are useful for fire propagation, where spillover can reach beyond immediately adjacent locations. In the empirical application (Section 6), p and λ_k are chosen from the sample space-time partial autocorrelation function (STPACF), dropping lags whose coefficients fall within the approximate 95% confidence bounds.

The process is stationary when

$$\rho\left(\sum_{k=1}^{p} \sum_{\ell=0}^{\lambda_k} \mathbf{\Phi}_{k,\ell}\mathbf{W}^{(\ell)}\right) < 1, \tag{2}$$

where $\rho(\cdot)$ is the spectral radius ([20]). The condition depends on both the coefficients and the spatial operators, so the structure of $\mathbf{W}^{(\ell)}$ under each support (Section 4) bears directly on it. We check it for the fitted models in Section 6.

2.2 Spatial Weight Matrix Construction

The weight matrix $\mathbf{W}$ expresses the strength of interaction between neighboring units ([14, 18, 20]). We consider Rook and Queen contiguity, with spatial lags up to third order to represent both short- and long-range dependence.

For the administrative support $\mathcal{A}$ ($N = 14$), adjacency follows from polygon contiguity: two regions are Rook-adjacent if they share an edge, and Queen-adjacent if they share an edge or a vertex. For the grid support $\mathcal{G}$ ($N = 51$), let (x_i, y_i) be the row-column coordinates of cell G_i. Rook contiguity of order k uses the Manhattan (L_1)

distance, $|x_i - x_j| + |y_i - y_j| = k$ ([22, 26]). Queen contiguity uses the Chebyshev (L_∞) distance, $\max(|x_i - x_j|, |y_i - y_j|) = k$, and therefore also admits diagonal neighbors ([18, 23]). Figure 1 shows the first-order neighborhoods. Higher-order lags ($k = 2, 3$) are built the same way and form further concentric rings around cell i.

The Queen criterion is used for estimation in Sections 5 and 6, because fire spread is not restricted to axis-aligned directions and diagonal neighbors belong to the local interaction. The Rook criterion is kept in Section 4 as a baseline to show how the neighborhood degree d_i affects sparsity.

This geometric construction defines a spatial interaction field which is much more homogeneous and structurally symmetric than irregular administrative topology. The regularity reduces the topological bias due to heterogeneous polygon geometries and helps to build more stable spatial operators.

To make the spatial units comparable and to keep the process stable, the resulting binary contiguity matrices $\mathbf{C}^{(k)}$ are row-standardized to obtain the final spatial weight operators $\mathbf{W}^{(k)}$. The standardized weights are given by

$$w_{ij}^{(k)} = \frac{c_{ij}^{(k)}}{\sum_{j=1}^{N} c_{ij}^{(k)}} \tag{3}$$

such that $\sum_{j=1}^{N} w_{ij}^{(k)} = 1$ for every spatial unit i. This normalization constrains the spatial eigenvalues and improves the numerical stability of the GSTAR estimation process.

3 Methodology

Scope of the support transformation and statistical model.

Two points define the scope of the analysis. First, the change between administrative and grid support is made *a priori*, as a data representation choice before model fitting, and it is not estimated by the model. A separate GSTAR model is fitted on each support. The Change of Support formalization in Section 3.1 is used to explain why this choice affects the fitted model, and it is not part of the estimation procedure. Second, the model is a linear GSTAR($p; \lambda$) process (Section 2.1) with zero-mean, finite-variance innovations, estimated by Ordinary Least Squares. The empirical application (Section 6) is limited to point estimation and out-of-sample forecast accuracy, with no formal hypothesis tests on the spatio-temporal coefficients.

3.1 The Change of Support Problem (COSP)

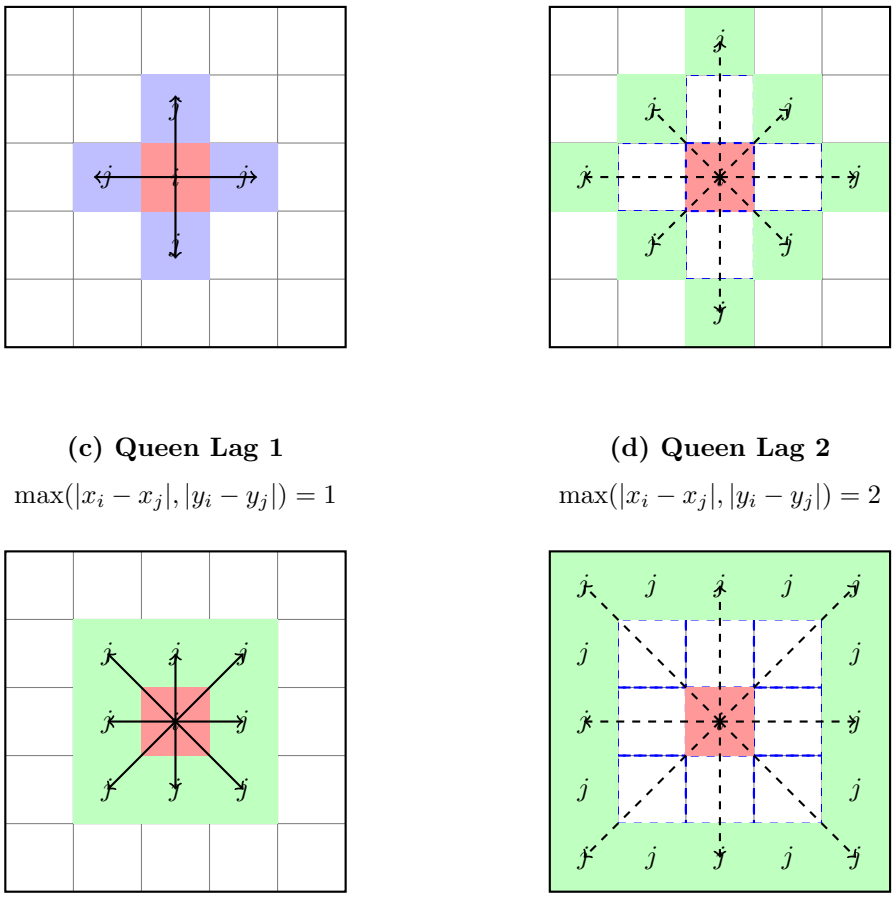
The Change of Support Problem (COSP) arises when data collected under one aggregation structure are moved to another spatial support. The support affects the dependence structure, the inference and the behavior of the fitted model. Advances in remote sensing and Geographic Information Systems (GIS) have made high-resolution spatial data widely available ([27]), but they have also made the choice of aggregation more consequential, in particular through the Modifiable Areal Unit Problem (MAUP).

(a) Rook Lag 1

$|x_i - x_j| + |y_i - y_j| = 1$

(b) Rook Lag 2

$|x_i - x_j| + |y_i - y_j| = 2$



(c) Queen Lag 1

$\max(|x_i - x_j|, |y_i - y_j|) = 1$

(d) Queen Lag 2

$\max(|x_i - x_j|, |y_i - y_j|) = 2$

Fig. 1: Neighbourhood structures generated by rook and queen contiguity on a regular grid. Panels (a) and (b) illustrate first-order and second-order rook contiguity based on the Manhattan distance. Panels (c) and (d) illustrate first-order and second-order queen contiguity based on the Chebyshev distance. The red cell denotes the target location i, while the neighbouring cells j represent locations included in the corresponding spatial lag structure.

MAUP is the sensitivity of statistical results to the size, scale and configuration of the spatial units ([28]). Because aggregated values depend on the partition, different supports can give different interaction patterns and different conclusions. MAUP is also related to the ecological fallacy, in which conclusions drawn from areal units do not hold for the underlying local process ([29]). The definition of the spatial units is

therefore a basic modeling decision, especially when local variability and interactions are to be preserved.

Let the variable of interest be a latent continuous spatio-temporal random field

$$\{Z(\boldsymbol{s}, t) : \boldsymbol{s} \in \mathcal{D}, t \in \mathcal{T}\},$$

where $\boldsymbol{s}$ is a location in the domain $\mathcal{D}$ and t is a discrete time index ([30]). Under the administrative support $\mathcal{A} = \{A_1, \ldots, A_{14}\}$, the value for region A_i at time t is obtained by spatial averaging,

$$Z(A_i, t) = \frac{1}{|A_i|} \int_{A_i} Z(\boldsymbol{s}, t)\, d\boldsymbol{s}, \tag{4}$$

where $|A_i| = \int_{A_i} d\boldsymbol{s}$ is the area of A_i.

Administrative regions are irregular and differ widely in size, so this averaging smooths the process unevenly. Large regions average out local extremes, which suppresses fine-scale variability and weakens local interactions. This also changes the covariance structure. Let $C(\boldsymbol{u}, \boldsymbol{v}) = \mathrm{Cov}(Z(\boldsymbol{u}, t), Z(\boldsymbol{v}, t))$ be the covariance function of the underlying process. The covariance between two administrative regions A_i and A_k is then

$$C(A_i, A_k) = \frac{1}{|A_i||A_k|} \int_{A_i} \int_{A_k} C(\boldsymbol{u}, \boldsymbol{v})\, d\boldsymbol{u}\, d\boldsymbol{v}. \tag{5}$$

Because the regions differ in shape and size, this integral distorts the decay of dependence with distance, and neighboring regions interact in an uneven way. For processes such as forest fires, dependence is strongest at short distances and decreases with distance, so averaging over large irregular areas can hide local spillover and bias the estimated dependence.

A regular grid reduces this problem. Nearby cells tend to behave similarly, and hotspot activity in one cell can influence adjacent cells through local fire propagation. For a small cell G_j of area $|G_j| \equiv \Delta$ and centroid $\boldsymbol{c}_{G_j}$, the block average is approximated by the value at the centroid,

$$Z(G_j, t) = \frac{1}{\Delta} \int_{G_j} Z(\boldsymbol{s}, t)\, d\boldsymbol{s} \approx Z(\boldsymbol{c}_{G_j}, t), \tag{6}$$

where $\mathcal{G} = \{G_1, \ldots, G_{51}\}$ is the set of grid cells. Moving from $N = 14$ administrative regions to $N = 51$ cells therefore represents local variability more evenly and gives more homogeneous neighborhoods, so that the spatial operators are sparser and more regular. Whether this improves the stability of the GSTAR estimates and the forecasts is examined in Sections 5 and 6.

3.2 Grid Support vs. Administrative Support

Two spatial representations are constructed over the study domain $\mathcal{D} \subset \mathbb{R}^2$. The first is the administrative support, a set of 14 irregular polygons (Figure 2(a)) that cover $\mathcal{D}$

and have disjoint interiors,

$$\mathcal{A} = \{A_1, A_2, \ldots, A_{14}\}, \qquad \bigcup_{i=1}^{14} A_i = \mathcal{D}.$$

Administrative boundaries are the usual choice because official statistics are released for these units. The units, however, differ widely in size and shape, which gives uneven neighborhood connectivity and weight matrices with little regular structure. Large units also average out local variability, as discussed in Section 3.1.

The second is a regular grid support (Figure 2(b)) obtained by dividing $\mathcal{D}$ into cells of fixed size $0.5^\circ \times 0.5^\circ$, about 55×55 km near the equator,

$$\mathcal{G} = \{G_1, G_2, \ldots, G_{51}\}.$$

This gives more units than the administrative support ($N = 51$ versus $N = 14$) and a uniform neighborhood structure by construction, a property formalized in Section 4.

The resolution balances spatial detail against data density. Finer cells would contain few or no hotspots over the observation period, producing sparse, zero-inflated series that are unsuitable for GSTAR estimation. Coarser cells would discard the local detail that motivates the change of support. The 0.5° resolution is therefore a practical compromise, not an optimum, and the sensitivity of the results to it is examined in Section 5.2.

For the weight matrices of the GSTAR model, the geometric centroid of each unit is used ([31]). Let $\boldsymbol{c}_{A_i}$ and $\boldsymbol{c}_{G_j}$ be the longitude–latitude coordinates of the centroids of region A_i and cell G_j, shown as red nodes in Figure 2. Moving from $\mathcal{A}$ to $\mathcal{G}$ thus changes not only the resolution but also the topology of the spatial operators.

3.3 Exploratory Spatial Data Analysis (ESDA)

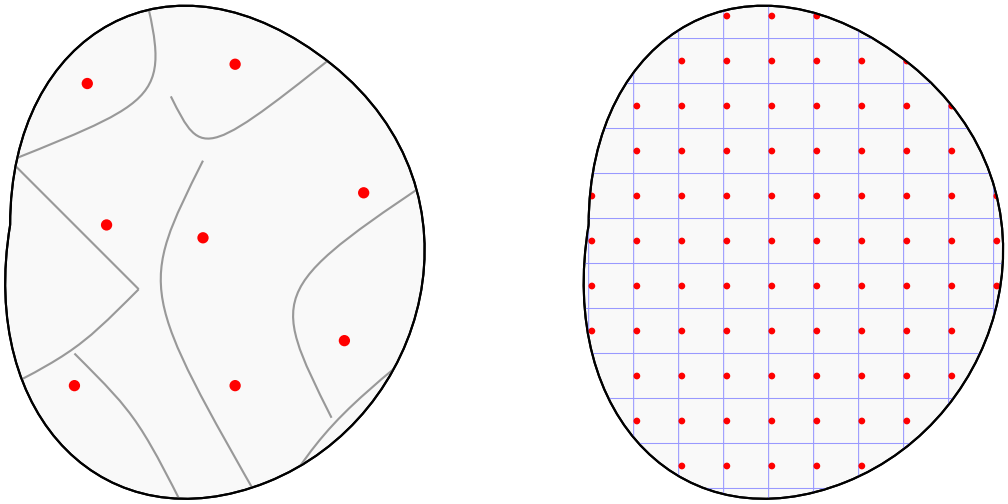
An Exploratory Spatial Data Analysis (ESDA) is used to examine how the spatial support affects the observed dependence structure ([32]). Global Moran's I gives one summary value for the whole study area and cannot show local heterogeneity ([33, 34]). We therefore use the Local Indicator of Spatial Association (LISA), or Local Moran's I, which splits the global statistic into location-specific components and identifies local clusters and spatial outliers ([35, 36]). Because our interest is in how the support changes local dependence, LISA is computed on both supports.

Let

$$\tilde{Z}_i = \frac{1}{T} \sum_{t=1}^{T} Z_i(t)$$

be the time-averaged observation of unit i. The Local Moran's I for unit i is ([33])

$$I_i = \frac{N(\tilde{Z}_i - \bar{Z})}{\sum_{k=1}^{N} (\tilde{Z}_k - \bar{Z})^2} \sum_{\substack{j=1 \\ j \neq i}}^{N} w_{ij} (\tilde{Z}_j - \bar{Z}), \tag{7}$$



(a) Administrative Support
Irregular polygons with aggregated support

(b) $0.5° \times 0.5°$ **Grid Support**
High-resolution regular grid support

Fig. 2: Conceptual illustration of the Change of Support Problem (COSP). Panel (a) shows the conventional administrative regions ($N = 14$), which mask local variations. Panel (b) depicts the high-resolution spatial discretization using a $0.5° \times 0.5°$ grid support ($N = 51$), providing a more granular topology for spatio-temporal modeling.

where $\bar{Z}$ is the mean over all N units and w_{ij} is the (i, j)th element of the row-standardized weight matrix $\boldsymbol{W}$. A positive I_i indicates a High–High or Low–Low cluster, and a negative I_i indicates a spatial outlier, High–Low or Low–High.

The two supports are expected to differ in what LISA can detect. On the administrative support $\mathcal{A}$ ($N = 14$), large irregular polygons smooth local variability, so localized hotspot activity may be hidden or the influence of isolated observations within a large unit may be inflated. On the grid support $\mathcal{G}$ ($N = 51$), cells of equal size at $0.5° \times 0.5°$ allow local interactions to be compared on the same footing and may reveal clusters that aggregation would hide. LISA is computed on the grid support, where the spatial units are comparable in size and a local analysis is meaningful. On the administrative support with only 14 units of very different sizes, local statistics have little power and cannot be compared fairly with the grid, so we do not interpret them as evidence about the support. The results are reported in Section 6 as a descriptive check on the spatial structure that the GSTAR operators have to represent.

4 Theoretical Properties of Grid-Based GSTAR Operators

This section studies the structure of the spatial operators produced under the grid support. A regular grid gives every cell a similar neighborhood, whereas administrative units do not, and this difference bears on computation, on the stability of the estimates and on the spectral behavior of the operator.

Let $\mathcal{G} = \{G_1, G_2, \ldots, G_N\}$ be a regular grid of N identical cells and let $\boldsymbol{W} = [w_{ij}] \in \mathbb{R}^{N \times N}$ be a row-standardized weight matrix, with $\mathcal{N}(G_i)$ the neighborhood of G_i under a finite-order contiguity rule. On a regular grid the degree $d_i = |\mathcal{N}(G_i)|$ is bounded: $d_i \leq 4$ for first-order Rook contiguity and $d_i \leq 8$ for first-order Queen contiguity. We state three results that follow from this bound: linear growth of the number of nonzero entries, a quasi-banded block structure, and a bounded spectral radius. None is a new result in matrix theory, as the remarks note. They are stated here for the GSTAR setting to explain the structural differences between the two supports that are examined in Sections 5 and 6.

4.1 Sparse Representation of Spatial Operators

Theorem 1 (Sparsity Growth) *Let $\boldsymbol{W} \in \mathbb{R}^{N \times N}$ be a spatial weight matrix on a regular grid with bounded neighborhood degree $d_{\max} < \infty$. Then $\operatorname{nnz}(\boldsymbol{W}) \leq N d_{\max} = \mathcal{O}(N)$, where $\operatorname{nnz}(\boldsymbol{W})$ is the number of nonzero entries of $\boldsymbol{W}$.*

Proof Each of the N rows has at most $d_{\max}$ nonzero entries, because a cell interacts only with its neighbors. Summing over rows gives $\operatorname{nnz}(\boldsymbol{W}) \leq N d_{\max}$, and $d_{\max}$ does not grow with N. □

Remark 1 The linear bound holds for any neighborhood graph with bounded degree. What is specific to the grid is that $d_{\max}$ is small, fixed and the same for all interior cells, whereas the degrees of administrative contiguity graphs are larger and more variable. The sparsity of the two supports used here is compared empirically in Section 6.

4.2 Block-Banded Structure of Grid-Based Operators

Proposition 2 (Quasi-Banded Structure) *Let $\boldsymbol{W}$ be the weight matrix of a regular two-dimensional grid under first-order Rook or Queen contiguity, with cells ordered row by row. Then $\boldsymbol{W}$ is block-tridiagonal, $\boldsymbol{W} = \operatorname{blocktridiag}(\boldsymbol{B}_{-1}, \boldsymbol{B}_0, \boldsymbol{B}_1)$, where each block $\boldsymbol{B}_k$ describes the interactions between grid rows that are k rows apart.*

Proof With row-by-row ordering, a cell has neighbors only in its own grid row and in the rows directly above and below. The nonzero entries of $\boldsymbol{W}$ therefore lie in the diagonal blocks and the blocks next to them. □

Remark 2 Block-banded structure under a fixed ordering is a standard property of local operators on regular grids, as in discretized differential operators and lattice Markov random

fields. It is stated here only to make explicit the form of the Rook and Queen operators used in this paper. For spatial lags of order $k > 1$, the number of block diagonals grows with k.

4.3 Spectral Radius of Row-Standardized Operators

Theorem 3 (Bounded Spectral Radius) *Let $\boldsymbol{W}$ be a row-standardized, non-negative weight matrix with zero diagonal. Then $\rho(\boldsymbol{W}) = 1$.*

Proof Row-standardization gives $\boldsymbol{W}\mathbf{1} = \mathbf{1}$, so 1 is an eigenvalue and $\rho(\boldsymbol{W}) \geq 1$. By the Gershgorin circle theorem, every eigenvalue lies in a disc centered at $w_{ii} = 0$ with radius $\sum_{j \neq i} w_{ij} = 1$, so $\rho(\boldsymbol{W}) \leq 1$. □

Remark 3 The result holds for any row-standardized weight matrix, on a grid or not, so it does not separate the two supports. What can differ is the spectral radius of the composite operator $\sum_{k,\ell} \boldsymbol{\Phi}_{k,\ell} \mathbf{W}^{(\ell)}$ in the stationarity condition (2), which also depends on the estimated coefficients. We check this condition on the fitted models in Section 6.

Together, these results describe the structure of the grid operator: linear sparsity growth and a block-banded form that follow from the bounded degree, and a spectral bound that holds for any row-standardized matrix. They give a structural basis for comparing the two supports. Whether this structure improves the stability of the estimates is assessed in Sections 5 and 6.

5 Simulation Study

The simulation study checks numerically how the change from grid to administrative support affects the structure of the GSTAR model, using a process whose true parameters are known. It examines three consequences of the Change of Support Problem (COSP): (i) distortion of the covariance structure (Section 3.1), (ii) loss of sparsity and regularity in the weight matrix (Section 4), and (iii) the effect of aggregation on the recovery of the spatial and temporal parameters. Forecast error is reported as well, but it is not the main focus.

The true Data Generating Process (DGP) evolves on the grid support $\mathcal{G}$ with $N_{\mathcal{G}} = 51$ units and follows a GSTAR(1; 1) model,

$$\boldsymbol{Z}_t^{\mathcal{G}} = \phi_{10} \boldsymbol{Z}_{t-1}^{\mathcal{G}} + \phi_{11} \boldsymbol{W}^{\mathcal{G}} \boldsymbol{Z}_{t-1}^{\mathcal{G}} + \boldsymbol{\varepsilon}_t, \tag{8}$$

where $\boldsymbol{\varepsilon}_t \sim \mathcal{N}(\mathbf{0}, \sigma^2 \boldsymbol{I})$ and $\boldsymbol{W}^{\mathcal{G}}$ is the first-order Queen weight matrix of the grid. We consider three scenarios: dominant spatial dependence (Scenario I, $\phi_{10} = 0.20$, $\phi_{11} = 0.60$), balanced dependence (Scenario II, $\phi_{10} = 0.40$, $\phi_{11} = 0.40$) and dominant temporal dependence (Scenario III, $\phi_{10} = 0.70$, $\phi_{11} = 0.10$). Because $\boldsymbol{W}^{\mathcal{G}}$ is row-standardized, $\phi_{10} + \phi_{11} = 0.8 < 1$ in all three scenarios, so the process is stationary. For each scenario we generate $T = 200$ observations, discard the first 50 as burn-in, and repeat the experiment for $M = 100$ Monte Carlo replications.

The grid-level series are then aggregated to the administrative support $\mathcal{A}$ with $N_{\mathcal{A}} = 14$ units,

$$\boldsymbol{Z}_t^{\mathcal{A}} = \boldsymbol{H}\boldsymbol{Z}_t^{\mathcal{G}}, \tag{9}$$

where $\boldsymbol{H} \in \mathbb{R}^{N_{\mathcal{A}} \times N_{\mathcal{G}}}$ is a row-stochastic aggregation matrix with entries

$$h_{ij} = \begin{cases} \dfrac{1}{|\mathcal{G}_i|}, & \text{if } j \in \mathcal{G}_i, \\ 0, & \text{otherwise.} \end{cases} \tag{10}$$

Here $\mathcal{G}_i = \{j : \boldsymbol{c}_{G_j} \in A_i\}$ is the set of grid cells whose centroid lies in region A_i, and $|\mathcal{G}_i|$ is its size. Every row of $\boldsymbol{H}$ sums to one, so $\boldsymbol{H}$ is a simple unweighted average of the cells assigned to each region.

5.1 Verification of Theoretical Properties

Covariance distortion.

Let $\widehat{\boldsymbol{\Sigma}}_{\mathcal{G}} \in \mathbb{R}^{N_{\mathcal{G}} \times N_{\mathcal{G}}}$ and $\widehat{\boldsymbol{\Sigma}}_{\mathcal{A}} \in \mathbb{R}^{N_{\mathcal{A}} \times N_{\mathcal{A}}}$ be the empirical covariance matrices of the grid-level and administrative-level series. They have different dimensions (51×51 and 14×14), so we first project the grid covariance onto the administrative support with the same operator $\boldsymbol{H}$,

$$\widetilde{\boldsymbol{\Sigma}}_{\mathcal{A}} = \boldsymbol{H}\,\widehat{\boldsymbol{\Sigma}}_{\mathcal{G}}\,\boldsymbol{H}^{\top}. \tag{11}$$

This is the covariance the grid process would have at administrative resolution if aggregation were a purely linear average. The distortion is measured by the Frobenius distance to the covariance estimated from the aggregated series,

$$D_{\text{cov}} = \left\| \widetilde{\boldsymbol{\Sigma}}_{\mathcal{A}} - \widehat{\boldsymbol{\Sigma}}_{\mathcal{A}} \right\|_F, \tag{12}$$

where larger values mean a stronger departure from simple averaging. In the simulations D_{cov} is large. The covariance decay stays localized under the grid support but is smoother and more diffuse after administrative aggregation. The effect is strongest in Scenario I, where the spatial component dominates and is averaged over large polygons, which weakens short-range dependence.

Sparsity.

For each support we compute the sparsity level $S(\boldsymbol{W}) = 1 - \text{nnz}(\boldsymbol{W})/N^2$ of the weight matrix. The grid matrix is much sparser and nearly banded, because a regular grid permits only local neighbors (Theorem 1 and Proposition 2). Administrative aggregation gives neighborhoods of very different size and a denser matrix.

Parameter recovery.

The GSTAR model is estimated separately on the two supports by OLS, and forecasts are evaluated over an out-of-sample horizon of $T_{\text{test}} = 24$. Table 1 gives the averages over $M = 100$ replications and Figure 3 shows the distribution of the estimates.

The grid support recovers the true coefficients closely, whereas the administrative support underestimates ϕ_{11} and overestimates ϕ_{10} in all three scenarios. The estimates

Table 1: Monte Carlo simulation results averaged over 100 replications. The table compares parameter recovery and forecasting accuracy between the original grid support ($N = 51$) and the aggregated administrative support ($N = 14$) under different spatio-temporal dependence scenarios.

Scenario	Support	True ϕ_{10}	True ϕ_{11}	Estimated $\hat{\phi}_{10}$	Estimated $\hat{\phi}_{11}$	RMSE
I (High Spatial)	Grid ($N = 51$)	0.20	0.60	0.202	0.597	**0.549**
	Administrative ($N = 14$)	0.20	0.60	0.508	0.303	0.998
II (Balanced)	Grid ($N = 51$)	0.40	0.40	0.401	0.401	**0.537**
	Administrative ($N = 14$)	0.40	0.40	0.607	0.211	0.995
III (High Temporal)	Grid ($N = 51$)	0.70	0.10	0.699	0.097	**0.532**
	Administrative ($N = 14$)	0.70	0.10	0.746	0.046	0.999

$\hat{\phi}_{10}$ and $\hat{\phi}_{11}$ are unit-free and can be compared across supports directly. Raw RMSE cannot, because the two series have different scales and variances. It is reported in Table 1 for completeness only, and forecast accuracy is compared on a standardized scale in Section 5.2. We therefore base the structural conclusion on parameter recovery, not on raw forecast error. The simulation indicates that the spatial support changes the dependence structure that the GSTAR model represents, so it should be treated as a modeling choice and not as preprocessing. The robustness checks below examine how far this conclusion depends on the simulation design.

5.2 Robustness Checks

Five checks examine whether the conclusions depend on the design of the simulation: (I) reversing the DGP onto the administrative support, (II–III) changing the grid resolution and the administrative partition, (IV) comparing with simpler baselines using a Diebold–Mariano (DM) test, and (V) timing the OLS fit. Forecast errors across supports are compared with the normalized RMSE (NRMSE), the RMSE divided by the training-period standard deviation of each unit, so that supports with different dimension and variance are comparable.

Check I: reversed DGP.

In the main design the DGP always lives on the grid, which could favor the grid mechanically. We therefore also generate the process on the administrative support (Delaunay contiguity) and obtain the grid series by disaggregation, so that each cell takes the value of its parent region. Under both directions the administrative support has equal or lower NRMSE (Table 2), so the design does not favor the grid.

Checks II–III: resolution and partition.

We repeat Scenario II with three grid resolutions ($N = 196, 49, 16$) and with a second administrative partition ($N = 28$). NRMSE is nearly constant across grid resolutions, and both administrative partitions stay below every grid (Table 3). The result therefore does not depend on the particular $N = 51$ grid or $N = 14$ partition.

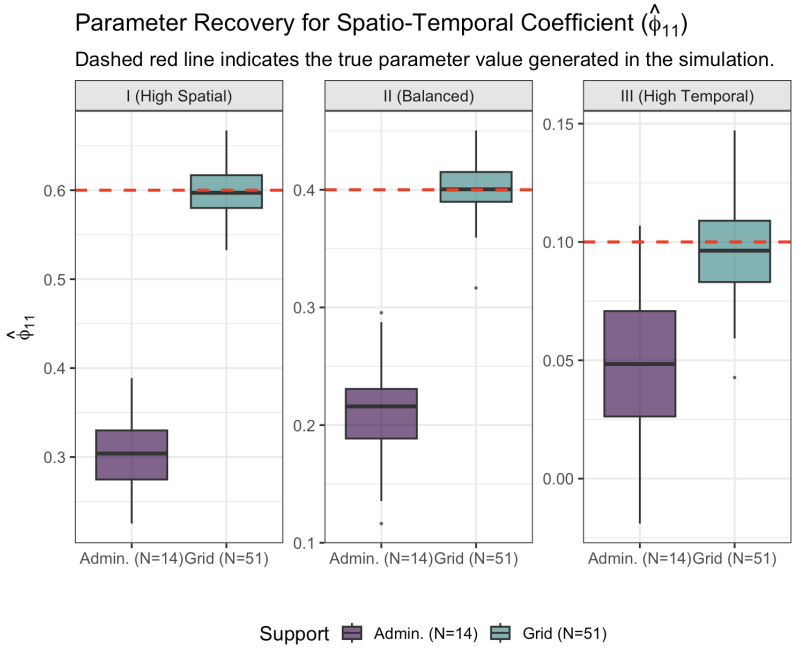


Fig. 3: Distribution of the estimated spatio-temporal parameter ($\hat{\phi}_{11}$) across 100 Monte Carlo replications for the three scenarios. The horizontal dashed lines represent the true DGP parameter values. The administrative support ($N = 14$) consistently underestimates the spatial dependence due to spatial smoothing.

Table 2: Check I: NRMSE under the two data-generating conditions ($M = 50$ replications).

Scenario	**Grid-true DGP**		**Administrative-true DGP**	
	Grid	Admin.	Grid	Admin.
I (High Spatial)	0.937	**0.751**	0.963	**0.915**
II (Balanced)	0.891	**0.717**	0.901	**0.878**
III (High Temporal)	0.725	**0.654**	0.728	**0.727**

Table 3: Checks II–III: NRMSE by grid resolution and administrative partition, Scenario II ($M = 50$ replications).

Support	N	**Mean NRMSE (SD)**
Grid (fine)	196	0.892 (0.011)
Grid (medium)	49	0.888 (0.019)
Grid (coarse)	16	0.883 (0.038)
Admin. (coarser)	14	0.706 (0.032)
Admin. (finer)	28	0.755 (0.025)

Check IV: baselines and DM test.

We compare GSTAR on both supports with an AR-only model ($\phi_{11} = 0$) and with naive persistence ($\hat{Z}_t = Z_{t-1}$). For the DM test on variance-standardized squared errors, the administrative forecasts are projected onto the grid with $\boldsymbol{H}$, so that both models are evaluated on the same units. GSTAR clearly beats persistence on both supports, while the AR-only model is only slightly worse than GSTAR on the grid, which shows that most of the predictive skill in this setting comes from the temporal term. The DM test is significant in every replication and favors the administrative model (Table 4). The raw-scale advantage of the grid in Table 1 therefore reflects the different scales of the two supports and not better forecasts.

Table 4: Check IV: NRMSE of GSTAR and baselines, and DM test of Grid against Administrative ($M = 50$ replications). A positive DM statistic favors the administrative model, and all differences are significant at $p < 0.05$ in every replication.

Scenario	GSTAR-Grid	GSTAR-Admin.	AR-only	Naive	Mean DM
I (High Spatial)	0.935	0.743	0.973	1.226	+50.8
II (Balanced)	0.890	0.710	0.907	1.069	+50.7
III (High Temporal)	0.724	0.649	0.725	0.785	+50.3

Check V: computation time.

The mean OLS fitting time grows with N regardless of the support, from 0.13 ms at $N = 14$ to 2.81 ms at $N = 196$ (20 repetitions), which is a modest cost at this size.

In summary, the findings on operator structure and parameter recovery do not depend on the DGP, the resolution or the partition, since they concern unit-free quantities. The finding that the grid forecasts better on the raw scale does not survive standardization. The main claim of the paper therefore rests on operator structure and parameter stability, and forecast accuracy is reported as a result that depends on the scale.

6 Results

6.1 Study Area and Data Acquisition

The empirical application uses West Kalimantan, Indonesia, a region on the equator that is a major source of forest and peatland fires. These fires are mostly caused by human activity such as land clearing, and they are sensitive to climate anomalies such as droughts linked to the El Niño–Southern Oscillation (ENSO). Fires in the region often spread to adjacent areas and last for long periods, so hotspot patterns show strong spatial and temporal dependence, which suits the GSTAR model.

The data are active-fire (hotspot) detections from the Fire Information for Resource Management System (FIRMS) of the National Aeronautics and Space Administration

(NASA), based on thermal anomalies observed by the Moderate Resolution Imaging Spectroradiometer (MODIS) and the Visible Infrared Imaging Radiometer Suite (VIIRS). The detections are aggregated weekly, giving $T = 268$ observations from January 2021 to early 2026. Weekly aggregation reduces noise and the share of zeros in the series. The response $Z_{i,t}$ is the number of hotspots detected in spatial unit i in week t.

Table 5 gives descriptive statistics for both supports. On the administrative support, activity is highly concentrated: Ketapang has the highest mean (45.12 hotspots per week, maximum 850), followed by Sintang and Kubu Raya, and most of the remaining regencies have low activity, so the distribution is strongly right-skewed. On the grid support, the most active cell has a mean of 18.23 and a maximum of 150, while the median and least active cells are much lower. Both supports contain the same 27,555 hotspots in total, so differences in model behavior come from the spatial support and not from the data.

Table 5: Descriptive statistics of weekly hotspot counts during 2021–2026 under administrative and grid-based spatial supports. The table highlights differences in the distribution, variability, and concentration of hotspot activity across the two spatial representations while preserving the same total number of hotspot observations.

Spatial Unit	**Count (N)**	**Mean**	**Std. Dev**	**Min**	**Max**	**Sum**
Panel A: Administrative Support (Selected Regencies)						
Pontianak	1	1.24	0.85	0	12	332
Ketapang	1	45.12	120.4	0	850	12,092
Sintang	1	28.34	75.21	0	420	7,595
Kuburaya	1	15.67	40.12	0	210	4,200
Other 10 Regencies (Avg)	10	12.45	30.15	0	180	3,336
Total Administrative	**14**	**20.56**	**53.33**	**0**	**850**	**27,555**
Panel B: Grid-Based Support (Statistical Summary)						
Highest-Activity Grid	1	18.23	45.10	0	150	4,885
Median-Activity Grid	1	5.12	12.45	0	45	1,372
Lowest-Activity Grid	1	0.05	0.12	0	1	13
Total Grid Network	**51**	**6.12**	**18.45**	**0**	**150**	**27,555**

Note: The total hotspot count remains identical under both spatial supports, indicating that the grid discretization preserves the overall hotspot intensity while redistributing its spatial concentration across smaller spatial units.

6.2 Spatial Discretization and Support Transformation

Before estimation, the hotspot detections were assigned to the two supports defined in Section 3.2 (Figure 4). The administrative support has $N = 14$ regencies and cities, whose sizes and shapes differ widely (Figure 4a). The grid support has $N = 51$ terrestrial cells of $0.5° \times 0.5°$, after excluding cells dominated by ocean (Figure 4b).

Each hotspot is counted in the region or cell that contains it, so the total count is the same on both supports. The two supports therefore differ only in how the same data are partitioned in space.

6.3 Local Indicators of Spatial Association (LISA)

LISA, as described in the ESDA subsection of Section 2, was computed for the average Fire Radiative Power (FRP) of each grid cell over the full observation period, with a row-standardized Rook weight matrix. Global Moran's I is 0.591 ($p < 0.001$), which indicates strong positive spatial autocorrelation. The cluster map (Figure 5) shows High–High clusters in the central part of the study area, Low–Low clusters mostly in the outer areas, and a few High–Low and Low–High outliers.

Table 6: Significant Local Moran's I clusters for average FRP on the grid support.

Grid ID	Cluster Type	Local Moran's I	Z-Score	p-value
25	High–High	2.534	2.466	0.0136
26	High–High	2.154	2.968	0.0030
36	High–High	1.656	3.164	0.0016
37	High–High	2.790	3.462	0.0005
38	High–High	2.694	2.622	0.0087
47	High–High	1.441	2.074	0.0381
48	High–High	1.647	2.191	0.0285
91	Low–Low	0.905	2.357	0.0184

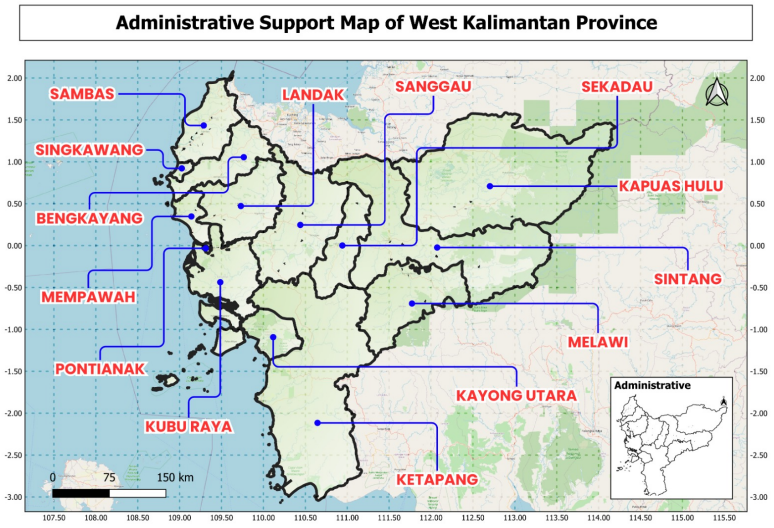
Seven of the eight significant clusters are High–High and one is Low–Low (Table 6). Fire intensity is therefore spatially clustered at the scale of neighboring cells, which is the kind of dependence that a neighborhood-based GSTAR operator can represent.

6.4 Model Fitting: Grid ($N = 51$) vs. Administrative ($N = 14$) Supports

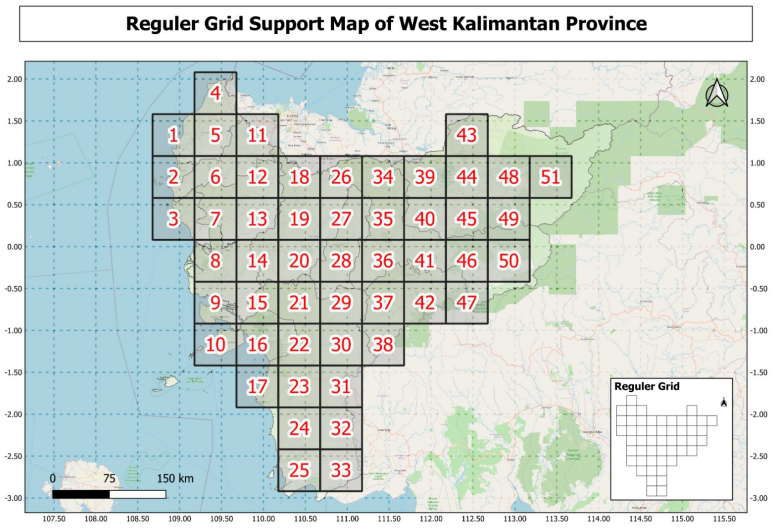
The administrative support is not proposed as a modeling choice. It is the status quo representation, since hotspot data are usually aggregated to official administrative units, and it serves as the benchmark for the grid. The comparison below shows with real data what the conventional representation loses.

6.4.1 Spatial Weight Construction and Structural Operator Properties

The spatial operators $\mathbf{W}^{(1)}, \mathbf{W}^{(2)}, \mathbf{W}^{(3)}$ use Queen contiguity up to the third lag, as constructed in Section 2.2, and are row-standardized. The lag order was chosen from the STPACF (Section 2.1). Figure 7 shows the operators for the grid support ($N = 51$), which stay near-banded as the lag order increases (Proposition 2).



(a)



(b)

Fig. 4: Spatial supports used in the study. (a) Administrative support of irregular regency and city polygons ($N = 14$). (b) Regular grid support of $0.5° \times 0.5°$ cells ($N = 51$).

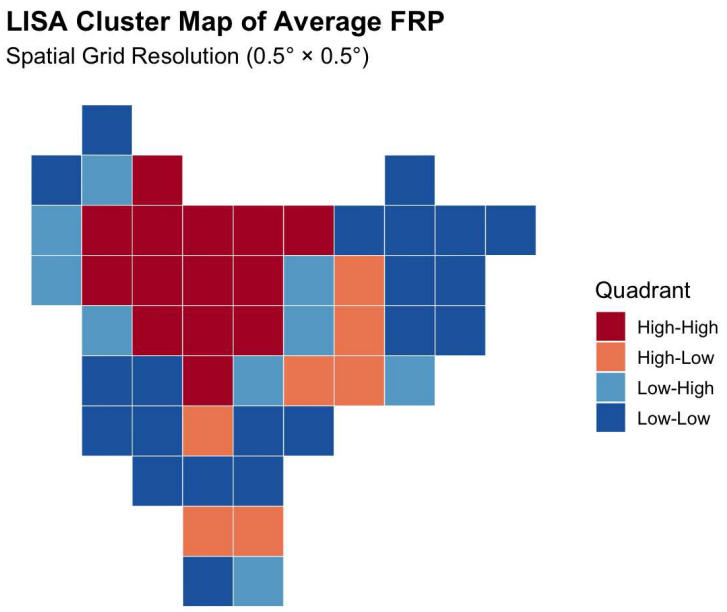


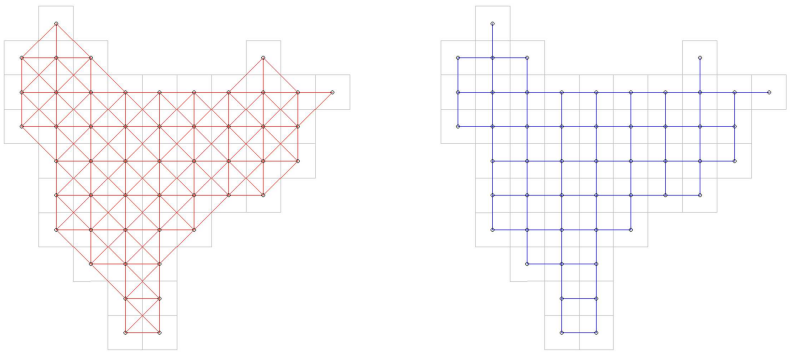
Fig. 5: LISA cluster map of average Fire Radiative Power (FRP) on the grid support (Rook contiguity). Red: High–High; dark blue: Low–Low; orange: High–Low; light blue: Low–High.

Table 7 reports the structure of the first-order operators on both supports: the density $D(\mathbf{W}) = \text{nnz}(\mathbf{W})/N^2$, the sparsity $S(\mathbf{W}) = 1 - D(\mathbf{W})$, and the node degree (Theorem 1 and Proposition 2). The spectral radius is not reported, because it equals one for any row-standardized matrix (Theorem 3).

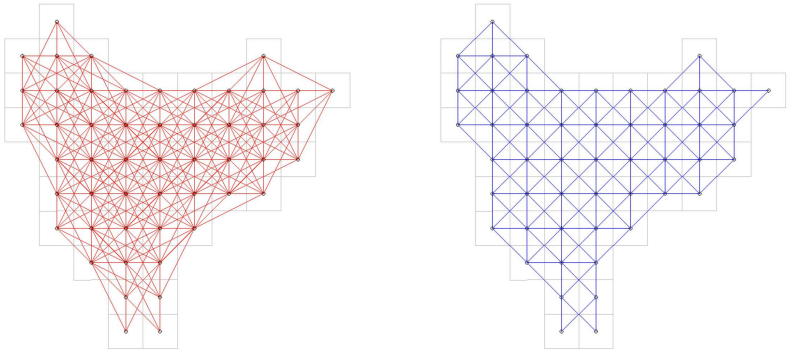
Table 7: Structural properties of the first-order spatial operators on the grid and administrative supports.

Property	**Grid** ($N = 51$)	**Administrative** ($N = 14$)
Nonzero entries (nnz)	408	96
Matrix density $D(\mathbf{W})$	0.157	0.490
Sparsity ratio $S(\mathbf{W})$	0.843	0.510
Average node degree	8.00	6.86
Degree variance	1.12	8.47

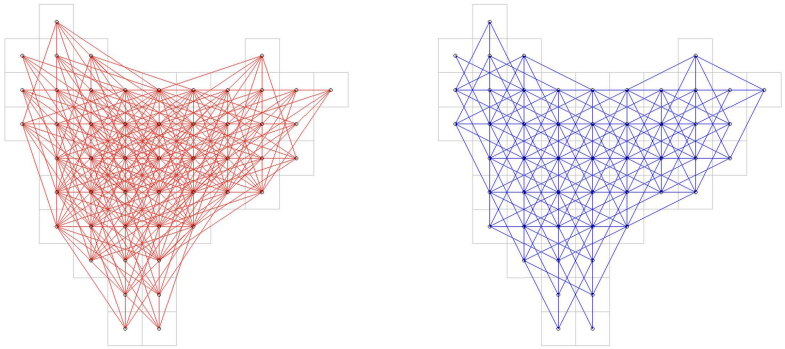
Although the grid has more units ($N = 51$ versus $N = 14$), its operator is sparser (density 0.157 versus 0.490) and its node degrees vary much less (degree variance 1.12 versus 8.47). This is the pattern expected from the bounded, homogeneous degree of a regular grid (Section 4).



(a)

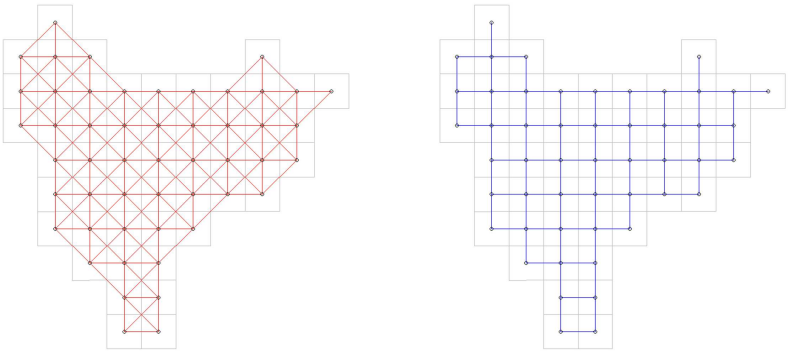


(b)

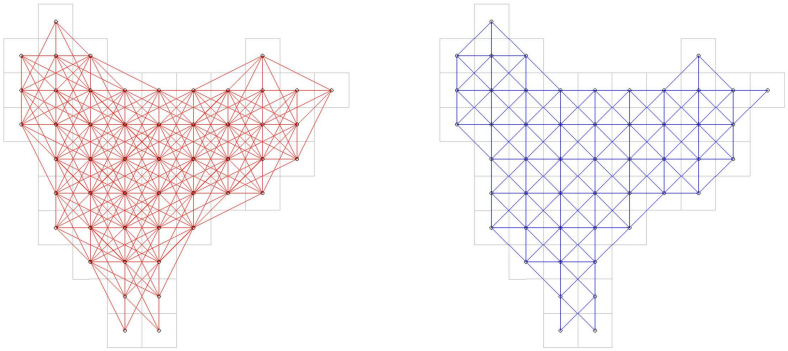


(c)

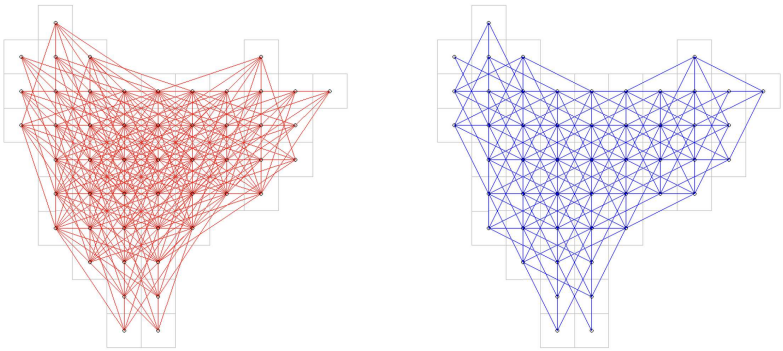
Fig. 6: Queen-contiguity spatial operators for the grid support ($N = 51$): (a) first-order, (b) second-order and (c) third-order spatial lag.



(a)



(b)



(c)

Fig. 7: Queen-contiguity spatial operators for the regular grid support ($N = 51$): (a) first-order spatial lag, (b) second-order spatial lag, and (c) third-order spatial lag. The regular grid topology generates symmetric and isotropic neighborhood expansion across increasing lag orders, preserving localized interaction structures and producing sparse near-banded spatial operators consistent with the theoretical properties established in Section 4.

6.4.2 Parameter Estimation Results

The empirical model is the GSTAR specification of Eq. (1) with temporal order $p = 2$ and spatial lags up to $\lambda_k = 3$, estimated by least squares in the VAR representation. The estimated coefficients are grouped into six components: the temporal effects at lags 1 and 2 ($\mathbf{\Phi}_{1,0}, \mathbf{\Phi}_{2,0}$), the spatial effects of orders 1 to 3 at temporal lag 1 ($\mathbf{\Phi}_{1,1}$–$\mathbf{\Phi}_{1,3}$), and the first-order spatial effect at temporal lag 2 ($\mathbf{\Phi}_{2,1}$). Table 8 gives the mean and standard deviation of each coefficient over the spatial units.

Table 8: Mean and standard deviation over spatial units of the estimated GSTAR coefficients on the grid and administrative supports.

Model Component	**Grid** ($N = 51$)		**Administrative** ($N = 14$)	
	Mean	Std. Dev	Mean	Std. Dev
$\mathbf{\Phi}_{1,0}$ (Temporal Lag 1)	0.31	0.22	0.34	0.25
$\mathbf{\Phi}_{1,1}$ (Spatial Lag 1)	0.27	0.24	0.29	0.28
$\mathbf{\Phi}_{1,2}$ (Spatial Lag 2)	0.19	0.21	0.23	0.26
$\mathbf{\Phi}_{1,3}$ (Spatial Lag 3)	0.13	0.18	0.18	0.23
$\mathbf{\Phi}_{2,0}$ (Temporal Lag 2)	0.22	0.20	0.26	0.24
$\mathbf{\Phi}_{2,1}$ (Spatial Lag 1)	0.17	0.19	0.21	0.22

The coefficients are similar in magnitude on the two supports, but the standard deviation over units is lower on the grid for every component, for example 0.24 versus 0.28 for $\mathbf{\Phi}_{1,1}$. The spatial coefficients decrease with the lag order on both supports, from 0.27 to 0.13 on the grid and from 0.29 to 0.18 on the administrative support, so higher-order effects are somewhat weaker on the grid. These differences are small. The standard deviations measure variation of the unit-specific estimates and not sampling uncertainty, and the number of units differs between the supports (51 versus 14). They therefore describe how homogeneous the estimated interactions are, and they are not a formal test of parameter stability. The simulation in Section 5.1, where the true parameters are known, is the main evidence on parameter recovery.

Stationarity.

The condition in Eq. (2) concerns the full set of estimated coefficient matrices together with the operators $\mathbf{W}^{(\ell)}$. It was not tested formally for the fitted models, so the forecasts below are predictions from the estimated models without a stationarity guarantee.

6.4.3 Model Fit Comparison

Table 9 reports the Akaike Information Criterion (AIC), the Bayesian Information Criterion (BIC), the Root Mean Square Error (RMSE), the Mean Absolute Error (MAE) and the Mean Absolute Percentage Error (MAPE) for both supports.

The grid model has lower RMSE, MAE and MAPE than the administrative model. These errors are computed on the original scale of each support, and the two series differ

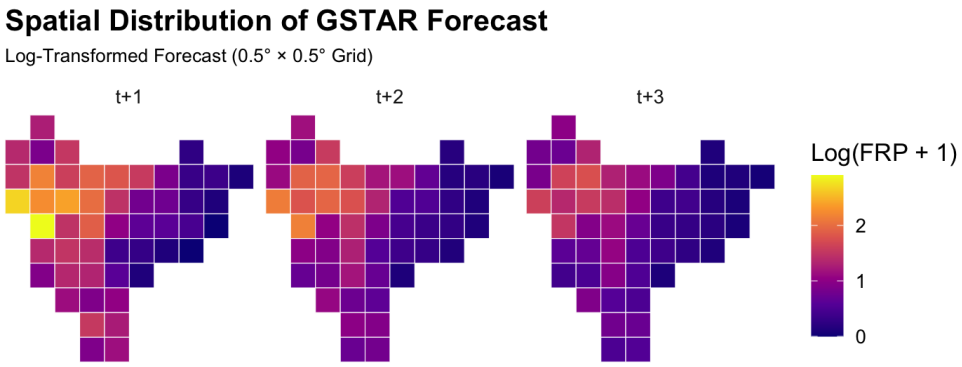
Table 9: Information criteria and forecast errors of the GSTAR models on the grid and administrative supports.

Model	AIC	BIC	RMSE	MAE	MAPE (%)
Grid ($N = 51$)	4,771	5,950	1.146	0.758	19.790
Administrative ($N = 14$)	2,112	2,381	1.252	0.943	24.458

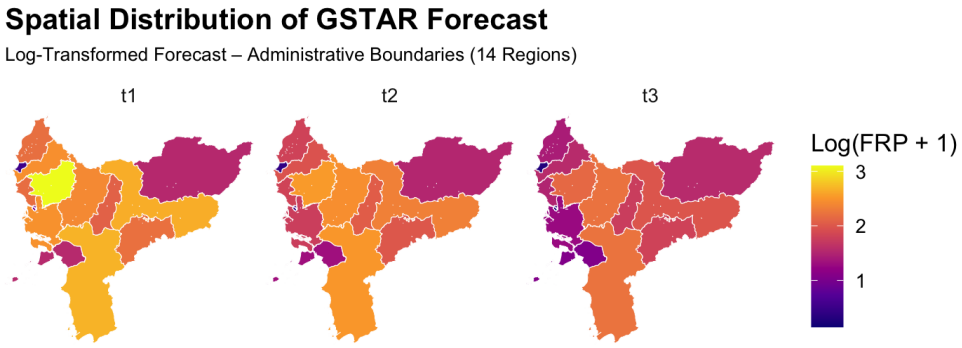
in variance because administrative values are aggregates of the grid cells. The errors are therefore not strictly comparable across supports. The simulations in Section 5.2 show that the ranking can reverse when errors are standardized by the variability of each unit, and a standardized comparison on the hotspot data was not done here. We therefore treat Table 9 as descriptive and not as evidence that the grid forecasts better. AIC and BIC are not compared either. The two models are fitted to different data matrices with different numbers of series, so their likelihoods are not comparable. The main empirical findings of this section concern the structure of the operators (Table 7) and the parameter estimates (Table 8), and forecast accuracy is a secondary and mixed result.

6.5 Spatio-Temporal Forecasting Performance

Out-of-sample forecasts of the GSTAR models were produced for the three periods $t+1$, $t+2$ and $t+3$ on both supports, the grid $\mathcal{G}$ ($N = 51$) and the administrative support $\mathcal{A}$ ($N = 14$). To limit the influence of extreme FRP values and to make the maps readable, forecasts are displayed on the scale $\log(\text{FRP} + 1)$. Figure 8 compares them.



(a) Grid-based forecast ($0.5^\circ \times 0.5^\circ$ resolution)



(b) Administrative-level forecast (14 regencies/cities)

Fig. 8: GSTAR forecasts for West Kalimantan at $t+1$, $t+2$ and $t+3$ on the grid support (upper panel) and the administrative support (lower panel), shown on the scale $\log(\text{FRP}+1)$.

The grid forecasts keep local high-intensity clusters across the horizon, whereas the administrative forecasts are visibly smoother. A smoother map does not by itself mean a more accurate forecast, so Table 10 reports RMSE and MAPE.

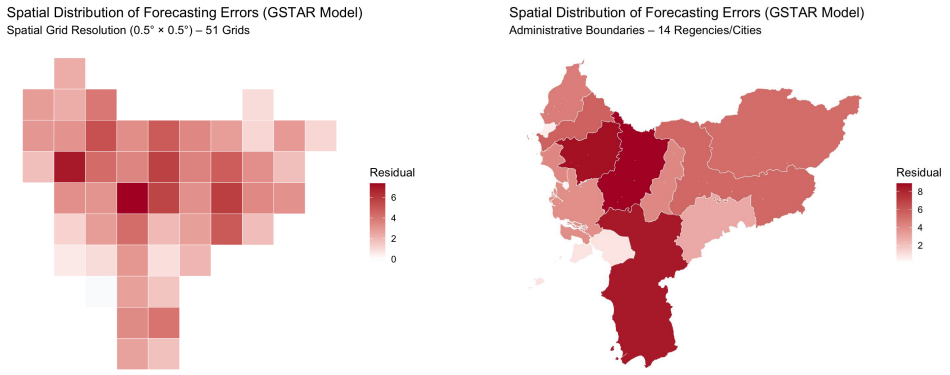
The grid has lower errors on both measures. As in Table 9, however, the errors are not standardized and the two supports have different variances, so the comparison is not conclusive (Section 5.2). We read the result as a description of the forecasts and not as proof that the grid is more accurate.

Table 10: Multi-step out-of-sample forecast errors on the grid and administrative supports (unstandardized).

Spatial Support	RMSE	MAPE (%)
Grid ($N = 51$)	8.72	21.35
Administrative ($N = 14$)	12.94	29.87

6.6 Spatial Distribution of Forecasting Errors

Aggregate measures such as RMSE and MAPE do not show whether the residuals contain systematic spatial bias, so Figure 9 maps the forecast residuals of the fitted GSTAR model on both supports.



(a) Regular grid support ($N = 51$) (b) Administrative support ($N = 14$)

Fig. 9: Spatial distribution of forecast residuals on (a) the grid support and (b) the administrative support.

On both supports the residuals are mostly centered around zero (red: underestimation, blue: overestimation). On the grid they are dispersed without clear spatial clustering, with a few isolated concentrations. On the administrative support they are smoother, which is expected after averaging over large polygons. The maps show no strong remaining spatial structure in the residuals, but they were not tested formally.

7 Discussion

The results indicate that the spatial support is a modeling choice with structural consequences for the GSTAR model and not a neutral preprocessing step. The evidence differs in strength across the parts of the study, and we summarize it in that order.

The strongest evidence comes from the simulations, where the true parameters are known. When the process lives on the grid and is aggregated to the administrative regions, the administrative model underestimates the spatial coefficient and overestimates the temporal one in all three scenarios (Table 1). Aggregation averages the process over large polygons, which weakens short-range dependence (Section 3.1), and this is consistent with part of the spatial effect appearing in the temporal coefficient. The robustness checks (Section 5.2) concern forecast error and do not re-examine parameter recovery. They show that the grid does not forecast better once errors are standardized.

The structure of the operators supports the same direction. The grid operator has more units but is sparser and has more homogeneous node degrees than the administrative operator (Table 7), as expected from the bounded degree of a regular grid (Theorem 1). The block-banded form (Proposition 2) implies that the operator can be stored and applied at a cost that grows linearly with N. This matters when GSTAR is applied to many locations, although at $N = 51$ the measured fitting time is small (Section 5.2). The estimated coefficients on the hotspot data (Table 8) are less dispersed over units on the grid, but the differences are small and descriptive, and they should not be read as a formal result on parameter stability. The LISA analysis shows spatial clustering of fire intensity at the scale of neighboring grid cells, which is the kind of dependence that a neighborhood-based operator can represent.

The forecasting results are mixed. Raw errors are lower on the grid for the real data (Tables 9 and 10), but the supports have different variances, and the simulations show that the ranking can reverse after standardization. We therefore do not claim a forecasting advantage for the grid. In practice a user may still prefer the administrative support when the forecast is needed at that level, and the question for the user is whether a finer support is needed for the purpose at hand.

Several limitations apply. First, the simulations aggregate with a simple unweighted average and use a first-order GSTAR process, so other aggregation rules and model orders may give different magnitudes. Second, the empirical analysis covers one region, one grid resolution and one administrative partition. Third, forecast accuracy on the hotspot data was not standardized, and the stationarity of the fitted models and the spatial autocorrelation of the residuals were not tested formally. Fourth, we compare the supports for a given model and do not estimate the support transformation itself, which would require a joint model of the process and the aggregation.

8 Conclusion

We compared a regular grid ($N = 51$) and the administrative regions ($N = 14$) as the spatial support of a GSTAR model for forest-fire hotspots in West Kalimantan. The support changes the structure of the spatial operators and the recovery of the model parameters. The grid operator is sparser and has more homogeneous node degrees, and in simulations with known parameters the grid recovers the spatial and temporal coefficients, whereas aggregation to administrative regions biases them. Forecast accuracy is a secondary and mixed result: raw errors favor the grid, but the advantage does not hold after standardizing by the variability of each unit.

For applications such as wildfire monitoring, the results suggest that the support should be chosen deliberately and that a finer regular support is worth considering when local spatial dependence matters. Future work could standardize the forecast comparison on real data, test the stationarity of the fitted models, use other aggregation rules and several resolutions, and extend the model with covariates, adaptive resolutions or nonlinear terms.

Declarations

Funding. This work was supported by the National Research and Innovation Agency (BRIN), Indonesia, through the *Riset dan Inovasi untuk Indonesia Maju* (RIIM) Kompetisi Gelombang X programme in 2026

Competing interests. The authors declare that they have no competing interests relevant to the content of this article.

Data availability. The hotspot data analysed in this study are publicly available from NASA FIRMS (https://firms.modaps.eosdis.nasa.gov). The processed datasets and code used for the simulations and analyses are available from the corresponding author on reasonable request.

Author contributions. Nur'ainul Miftahul Huda: Conceptualization, Methodology, Software. Yundari: Data curation, Investigation, Validation. Nurfitri Imro'ah: Data curation, Investigation, Visualization. Rahmi Hidayati: Validation, Writing – review & editing. Kartika Sari: Validation, Writing – review & editing. Muhammad Yahya Ayyash: Visualization, Software, Formal analysis. All authors read and approved the final manuscript.

References

[1] Cressie, N., Wikle, C.K.: Statistics for Spatio-Temporal Data. John Wiley and Sons, New York (2011)

[2] Wikle, C.K.: Modern perspectives on statistics for spatio-temporal data. WIREs Computational Statistics **7**(1), 86–98 (2015) https://doi.org/10.1002/wics.1341

[3] Clarke, H., Nolan, R.H., De Dios, V.R., Bradstock, R., Griebel, A., Khanal, S., Boer, M.M.: Forest fire threatens global carbon sinks and population centres under rising atmospheric water demand. Nature Communications **13**(1), 7161 (2022) https://doi.org/10.1038/s41467-022-34966-3

[4] Ghorbanzadeh, O., Blaschke, T., Gholamnia, K., Aryal, J.: Forest fire susceptibility and risk mapping using social/infrastructural vulnerability and environmental variables. Fire **2**(3), 50 (2019) https://doi.org/10.3390/fire2030050

[5] Hein, L., Spadaro, J.V., Ostro, B., Hammer, M., Sumarga, E., Salmayenti, R., Boer, R., Tata, H., Atmoko, D., Castañeda, J.-P.: The health impacts of indonesian

peatland fires. Environmental Health **21**(1), 62 (2022) https://doi.org/10.1186/s12940-022-00872-w

[6] Kiely, L., Spracklen, D.V., Arnold, S.R., Papargyropoulou, E., Conibear, L., Wiedinmyer, C., Knote, C., Adrianto, H.A.: Assessing costs of indonesian fires and the benefits of restoring peatland. Nature Communications **12**(1), 7044 (2021) https://doi.org/10.1038/s41467-021-27353-x

[7] Carta, F., Zidda, C., Putzu, M., Loru, D., Anedda, M., Giusto, D.: Advancements in forest fire prevention: A comprehensive survey. Sensors **23**(14), 6635 (2023) https://doi.org/10.3390/s23146635

[8] Cao, Y., Zhou, X., Yu, Y., Rao, S., Wu, Y., Li, C., Zhu, Z.: Forest fire prediction based on time series networks and remote sensing images. Forests **15**(7), 1221 (2024) https://doi.org/10.3390/f15071221

[9] Sloan, S., Tacconi, L., Cattau, M.E.: Fire prevention in managed landscapes: Recent success and challenges in indonesia. Mitigation and Adaptation Strategies for Global Change **26**(7), 32 (2021) https://doi.org/10.1007/s11027-021-09965-2

[10] Kumar, R., Bhanu, M., Mendes-Moreira, J., Chandra, J.: Spatio-temporal predictive modeling techniques for different domains: A survey. ACM Computing Surveys **57**(2), 1–42 (2024) https://doi.org/10.1145/3696661

[11] Tsui, T., Derumigny, A., Peck, D., Timmeren, A., Wandl, A.: Spatial clustering of waste reuse in a circular economy: A spatial autocorrelation analysis on locations of waste reuse in the netherlands using global and local moran's i. Frontiers in Built Environment **8**, 954642 (2022) https://doi.org/10.3389/fbuil.2022.954642

[12] Qian, S., Zhu, X.: Meshhstgt: hierarchical spatio-temporal fusion for mesh network traffic forecasting. Scientific Reports **15** (2025) https://doi.org/10.1038/s41598-025-01943-x

[13] Borovkov, A.A., Borovkov, K.A.: Asymptotic Analysis of Random Walks: Heavy-Tailed Distributions. Encyclopedia of Mathematics and its Applications, vol. 118. Cambridge University Press, ??? (2008). https://doi.org/10.1017/CBO9780511721397

[14] Mukhaiyar, U., Mahdiyasa, A.W., Sari, K.N., Noviana, N.T.: Risk Mapping of Groundwater Level in Peatland Area Utilizing a Spatio-Temporal Model with Weight Constructed Based on Minimum Spanning Tree. Research Square. Preprint (2024). https://doi.org/10.21203/rs.3.rs-4119220/v1

[15] Mukhaiyar, U., Huda, N.M., Sari, R.R.K.N., Pasaribu, U.S.: Modeling dengue fever cases by using gstar(1;1) model with outlier factor. Journal of Physics: Conference Series **1366**(1), 012122 (2019) https://doi.org/10.1088/1742-6596/1366/1/012122

[16] Huda, N.M., Imro'ah, N., Hidayati, R., Sari, K.: Combining iot and time series model for minute-level outlier detection in wind speed forecasting. CAUCHY: Jurnal Matematika Murni dan Aplikasi **10**(2) (2025) https://doi.org/10.18860/cauchy.v10i2.35768

[17] Huda, N.M., Imro'ah, N.: Determination of the best weight matrix for the generalized space time autoregressive (gstar) model in the covid-19 case on java island, indonesia. Spatial Statistics **56**, 100734 (2023) https://doi.org/10.1016/j.spasta.2023.100734

[18] Huda, N.M., Imro'ah, N.: Covid-19 case modeling in java island using a spatial model, gstar(1;1), with modified spatial weights: Queen contiguity weight matrix. In: AIP Conference Proceedings, p. 090009. American Institute of Physics, ??? (2024). https://doi.org/10.1063/5.0201676

[19] Mukhaiyar, U., Mahdiyasa, A.W., Prastoro, T., Pasaribu, U.S., Sari, K.N., Indratno, S.W., Soekarno, I., Choesin, D.N., Ismail, I., Rosleine, D., Qoyyimi, D.T.: The generalized star modelling with three-dimensional of spatial weight matrix in predicting the indonesia peatland's water level. Environmental Sciences Europe **36**, 180 (2024) https://doi.org/10.1186/s12302-024-00979-6

[20] Yundari, Y., Huda, N.M., Pasaribu, U.S., Mukhaiyar, U., Sari, K.N.: Stationary process in gstar(1;1) through kernel function approach. In: AIP Conference Proceedings, vol. 2268, p. 020010. American Institute of Physics, ??? (2020). https://doi.org/10.1063/5.0016808

[21] Yundari, Pasaribu, U.S., Mukhaiyar, U., Heriawan, M.N.: Spatial weight determination of gstar(1;1) model by using kernel function. Journal of Physics: Conference Series **1028**(1), 012223 (2018) https://doi.org/10.1088/1742-6596/1028/1/012223

[22] Ayyash, M.Y., Huda, N.M., Imro'ah, N.: The gstar (1;1) modelling with three combination of the grid sizes and spatial weight matrix in forest fires cases. JTAM (Jurnal Teori dan Aplikasi Matematika) **9**(1), 134–146 (2025) https://doi.org/10.31764/jtam.v9i1.27543

[23] Pratiwi, H., Imro'ah, N., Huda, N.M., Ayyash, M.Y.: Comparison of weight matrix in hotspot modeling in west kalimantan using the gstar method. Jurnal Matematika UNAND **14**(1), 31–45 (2025) https://doi.org/10.25077/jmua.14.1.31-45.2025

[24] Imro'ah, N., Huda, N.M., Pratiwi, H., Ayyash, M.Y.: Spatio-temporal modeling of fire hotspots using gstar(1;1) model with meteorology-based weight matrices. Hacettepe Journal of Mathematics and Statistics **54**(6), 2525–2542 (2025) https://doi.org/10.15672/hujms.1726843

[25] Fitriyana, G., Imro'ah, N., Huda, N.M.: Interpolation of fire radiative power based on gstar model predictions with queen contiguity weights using ordinary kriging. CAUCHY: Jurnal Matematika Murni dan Aplikasi **11**(1) (2026) https:

//doi.org/10.18860/cauchy.v11i1.37462

[26] Ayyash, M.Y., Huda, N.M., Imro'ah, N., Pratiwi, H.: Analysis of forest fire cases using gstar(1;1) model with spatial rook contiguity weights matrix in west kalimantan. Jurnal Matematika UNAND **15**(2), 259–273 (2026) https://doi.org/10.25077/jmua.15.2.259-273.2026

[27] Rawson, A.D., Brito, M., Sabeur, Z.: Geospatial mining of massive ais data for strategic management of maritime navigation safety: Methodological and policy considerations. In: Royal Institute of Navigation Conference 2021, Virtual Conference (2021). In Press

[28] Woodard, J.B., Mirus, B.B., Wood, N.J., Allstadt, K.E., Leshchinsky, B.A., Crawford, M.M.: Slope unit maker (sumak): an efficient and parameter-free algorithm for delineating slope units to improve landslide modeling. Natural Hazards and Earth System Sciences **24**, 1–12 (2024) https://doi.org/10.5194/nhess-24-1-2024

[29] Alexandridis, T.K., Katagis, T., Gitas, I.Z., Silleos, N.G., Eskridge, K.M., Gritzas, G.: Investigation of aggregation effects in vegetation condition monitoring at a national scale. International Journal of Geographical Information Science **24**(4), 507–521 (2010)

[30] Bečić, D., Pažur, A.: Exploring spatial patterns of urban heat islands in zagreb. In: REAL CORP 2025 Proceedings. CORP Conference, ??? (2025). https://doi.org/10.48494/REALCORP2025.8125

[31] Cheng, T., Haworth, J., Anbaroglu, B., Tanaksaranond, G., Wang, J.: Spatio-temporal data mining. In: Handbook of Regional Science, pp. 1691–1709. Springer, ??? (2021)

[32] Chasco, C.: Basic spatial exploratory spatial data analysis in geoda software. Preprints (2025) https://doi.org/10.20944/preprints202503.2044.v2 . Preprint, version 2

[33] Chen, Y.: An analytical process of spatial autocorrelation functions based on moran's index. PLOS ONE **16**(4), 0249589 (2021) https://doi.org/10.1371/journal.pone.0249589

[34] Anselin, L.: The moran scatterplot as an esda tool to assess local instability in spatial association. In: Spatial Analytical Perspectives on GIS, pp. 111–125. Routledge, ??? (1996)

[35] Nurdiansyah, R.: Spatial analysis of hepatitis a case distribution using moran's index and lisa (local indicator of spatial association). SPMS (Scientific Journal of Public Health and Medical Studies) **2**(1) (2025) https://doi.org/10.61511/spms.v2i1.2025.1758

[36] Seya, H.: Global and local indicators of spatial associations. In: Spatial Analysis and Location Modeling in Urban and Regional Systems. Elsevier, ??? (2020). https://doi.org/10.1016/B978-0-12-813127-5.00003-5